Seasonal variations in composition and sources of atmospheric ultrafine particles in urban Beijing based on near-continuous measurements

Xiaoxiao Li[1,2], Yijing Chen[1], Yuyang Li[1], Runlong Cai[3], Yiran Li[1], Chenjuan Deng[1], Jin Wu[1], Chao Yan[3,4], Hairong Cheng[2], Yongchun Liu[4], Markku Kulmala[3,4], Jiming Hao[1], James N. Smith[5*], and Jingkun Jiang[1*]

[1] State Key Joint Laboratory of Environment Simulation and Pollution Control, School of Environment, Tsinghua University, 100084 Beijing, China

[2] School of Resources and Environmental Sciences, Wuhan University, 430072 Wuhan, China

[3] Institute for Atmospheric and Earth System Research / Physics, Faculty of Science, University of Helsinki, 00014 Helsinki, Finland

[4] Aerosol and Haze Laboratory, Beijing Advanced Innovation Center for Soft Matter Science and Engineering, Beijing University of Chemical Technology, 100029 Beijing, China

[5] Chemistry Department, University of California, Irvine, CA 92697, USA

Correspondence to: Jingkun Jiang (jiangjk@tsinghua.edu.cn) and James N. Smith (jimsmith@uci.edu)

Abstract. Understanding the composition and sources of atmospheric ultrafine particles (UFPs) is essential in evaluating their exposure risks. It requires long-term measurements with high time resolution, which are to date scarce. We performed near-continuous measurements of UFP composition during four seasons in urban Beijing using a thermal desorption chemical ionization mass spectrometer, accompanied by real-time size distribution measurements. We found that UFPs in urban Beijing are dominated by organic components, varying seasonally from 68 to 81%. CHO organics (i.e., molecules containing carbon, hydrogen, and oxygen) are the most abundant in summer, while sulfur-containing organics, some nitrogen-containing organics, nitrate, and chloride are the most abundant in winter. With the increase of particle diameter, the contribution of CHO organics decreases, while that of sulfur-containing and nitrogen-containing organics, nitrate, and chloride increase. Source apportionment analysis of the UFP organics indicates contributions from cooking and vehicle sources, photooxidation sources enriched in CHO organics, and aqueous/heterogeneous sources enriched in nitrogen- and sulfur-containing organics. The increased contributions of cooking, vehicle, and photooxidation components are usually accompanied by simultaneous increases in UFP number concentrations related to cooking emission, vehicle emission, and new particle formation, respectively. While the increased contribution of the aqueous/heterogeneous composition is usually accompanied by the growth of UFP mode diameters. The highest UFP number concentrations in winter are due to the strongest new particle formation, the strongest local primary particle number emissions, and the slowest condensational growth of UFPs to larger sizes. This study provides a comprehensive understanding of urban UFP composition and sources and offers valuable datasets for the evaluation of UFP exposure risks.

1. Introduction

Ultrafine particles (UFPs, particles with diameters smaller than or equal to 100 nm) have significant effects on human health (HEI, 2013; Ohlwein et al., 2019; WHO, 2013) and global climate (Kulmala et al., 2004; Pierce and Adams, 2007). Their human exposure risks and climate effects are highly related to their composition and size (Oberdorster et al., 2005; Pierce and Adams, 2007). To better evaluate the exposure risks of UFPs and to formulate corresponding air quality guidelines, the World Health Organization made several recommendations to guide measurements and regulations of UFPs in 2021 (Organization, 2021). They emphasized that local understanding of UFP origins and their chemical composition are scarce in most parts of the world.

Current field studies of atmospheric UFP composition and their source apportionment are mostly based on offline sampling. These measurements usually use a size-resolving impactor to collect UFPs on filters for tens of hours to several days (Cabada et al., 2004; Cass et al., 2000; Ham and Kleeman, 2011; Herner et al., 2005; Kleeman et al., 2009; Massling et al., 2009; Xue et al., 2019; Xue et al., 2020a; Xue et al., 2020b; Zhao et al., 2017). They found that organic carbon, sulfate, and nitrate could account for 50-90% of the detected compounds, and the composition could vary greatly with UFP sizes due to different sources and atmospheric evolutions (Cabada et al., 2004; Herner et al., 2005; Massling et al., 2009). For source apportionment, the Chemical Mass Balance analysis was often used which relies heavily on the source profiles and the limited numbers of molecular markers (Ham and Kleeman, 2011; Kleeman et al., 2009; Xue et al., 2019). The identified sources include meat cooking, gasoline, diesel, motor oil, and wood burning. However, these offline explorations can not capture the high temporal variability in size-resolved UFP composition and sources, nor can they distinguish primary UFPs from secondary sources, e.g., new particle formation, due to the lack of tracers and composition profiles for secondary sources. Simultaneous real-time measurements of UFP composition and size distributions are needed to accurately identify both primary and secondary sources.

Using a thermal desorption chemical ionization mass spectrometer (TDCIMS), the size-resolved composition of UFPs can be measured with a resolution of tens of minutes (Li et al., 2021; Smith et al., 2004). Previously, it has been used in a number of sites for short-term measurements and found distinct characteristics for UFPs in urban (Li et al., 2022a; Li et al., 2021; Smith et al., 2008; Smith et al., 2005), rural (Lawler et al., 2020; Smith et al., 2010), and remote areas (Glicker et al., 2019; Lawler et al., 2018; Lawler et al., 2021; Lawler et al., 2014). For instance, UFPs in urban areas have more nitrogen- and sulfur-containing organics (Smith et al., 2005; Winkler et al., 2012), while those at forest sites have more CHO organics (i.e., molecules containing carbon, hydrogen, and oxygen) (Glicker et al., 2019; Lawler et al., 2018). With these near-continuous measurements, unique sources such as fungal bursts (Lawler et al., 2020) and sea-salt nanoparticles (Lawler et al., 2014) were identified and the mechanisms of new particle formation were examined (Li et al., 2022a). Source apportionment analysis was performed for the high time-resolution TDCIMS results in Amazon Basin to isolate

anthropogenic UFPs from background UFPs (Glicker et al., 2019). These analyses mainly focused on short-term analysis covering several weeks. To address the UFP composition and sources from a more comprehensive view, there is an urgent need for long-term and high-time-resolution measurements in diverse environments.

The primary and secondary sources of particles in urban atmospheres usually show significant seasonal characteristics. Thus, addressing the seasonal variations of UFPs, as well as their governing factors, is fundamental to evaluating their long-term impacts. For fine particles in Beijing, coal combustion is more abundant in winter due to domestic heating in the surrounding regions (Sun et al., 2015; Zhang et al., 2013), biomass burning is more abundant in harvest seasons (Zhang et al., 2008), and dust storms are more frequent in spring (Xu et al., 2020; Zhang et al., 2013). Besides these primary sources, previous studies on larger particles showed higher oxidation states of organic aerosols in summer due to stronger photochemical processes (Hu et al., 2017; Ma et al., 2022; Sun et al., 2018). However, considering the short lifetime of UFPs, seasonal variations of the composition and sources of UFPs are likely different. For example, as an important source of UFPs, new particle formations in Beijing were observed to be the weakest in summer and strongest in winter due to temperature variations (Deng et al., 2020; Li et al., 2020; Wu et al., 2007). Similar to Beijing, seasonal variations of UFP composition based on high time-resolution measurements are also scarce for other atmospheric sites.

Here, we performed near-continuous measurements of UFP composition and size distributions over four seasons in a typical megacity of Beijing with ~22 million people. The UFP composition, its size dependence, and seasonal variability were analyzed. Several molecular markers from cooking and vehicle emissions were identified. These markers were combined with the Positive Matrix Factorization (PMF) analysis to address contributions from primary and secondary sources of UFPs. The aerosol General Dynamic Equation (GDE) was used to quantify the emission rates of primary UFPs and the formation rates of secondary UFPs. The driving factors for the seasonal variations of UFP composition and number concentrations were identified.

2. Methods

2.1 Field measurements.

The sampling site is on the fifth floor of a building on the west campus of Beijing University of Chemical Technology (39°94′N, 116°30′E) (Liu et al., 2020). The site is a typical urban site, surrounded by residential and commercial buildings. Three trafficked roads are 130~565 m away from the sites. UFP composition, particle number-size distribution, trace gases, and meteorological conditions were measured over four seasons between Dec. 2019 and Aug. 2021. An overall of 149 days' TDCIMS measurements were used for analysis, with at least three weeks' data for each season. Details of the sampling periods are described in Table S1.

UFP composition was measured by the TDCIMS using the "bulk collection mode" (Li et al., 2021;

108   Smith et al., 2004). The TDCIMS collects pre-charged particles on a high voltage-biased Pt filament
109   and then vaporizes the particles for analysis by a chemical ionization high-resolution time-of-flight
110   mass spectrometer (CI-HTOF, Aerodyne Research Inc. and Tofwerk AG). The particle electrostatic
111   collection efficiency on the filament decreases rapidly with increasing particle size due to decreased
112   electrical mobility, ensuring that the collected particle mass is mainly from UFPs (Li et al., 2021).
113   During the particle evaporation, an electrical current is applied to the metal filament to an estimated
114   temperature of ~600 °C within a minute. The observed compounds can be desorbed thoroughly within
115   the heating periods as indicated by the desorption profile. Using O_2^- as the reagent ion, sulfate, nitrate,
116   chloride, and most of the oxygenated organics can be measured, while black carbon, hydrocarbon
117   compounds, and bases such as ammonium and aminium are less likely to be detected due to lower
118   sensitivity. Every sampling cycle is followed by a background cycle where no voltages are applied to
119   the Pt filament for particle collection. The signals from the background cycle are subtracted from the
120   sampling cycle to exclude minor influences from the gas phase compounds. Each analysis cycle
121   (including a sample and a background cycle) is set to be 10-40 min, depending on the estimated sample
122   mass. The detailed principles, operations, and quantifications of the TDCIMS are the same as the "bulk
123   collection mode" described in our previous study (Li et al., 2021).

124   The particle number size distributions from 1 nm to 10 μm were measured using a home-built particle
125   size distribution system (PSD, 3 nm–10 μm) and a diethylene glycol scanning mobility particle
126   spectrometer (DEG-SMPS, 1–7.5 nm). The configuration and operation of the PSD are the same as
127   described in our previous studies (Cai et al., 2017). The time resolution of the measurement is 5 min.
128   The number and mass concentrations of atmospheric UFPs were estimated via the integration of size
129   distribution measurements, assuming spherical particles with a density of 1.4 g cm^{-3}.

130   Other parameters used in this study include the meteorological conditions measured by the
131   meteorology stations (AWS310, Vaisala Inc., Finland) and trace gases measured by the trace gas
132   analyzers (TGA, Thermo Fisher). The mixing layer height (MLH) was estimated from the vertical
133   profiles measured by a ceilometer (CL51, Vaisala Inc., Finland) and a three-step idealized-profile
134   method was used to estimate the MLH (Eresmaa et al., 2012).

135   **2.2 Source apportionment of UFP composition.**
136   The Igor-based interface SoFi (solution finder, version 6.5) and ME-2 (Canonaco et al., 2013) were
137   used for the PMF analysis to analyze the sources of organics in UFPs. The integrated thermal
138   desorption signals of organic peaks with m/z between 100 and 300 measured by the TDCIMS were
139   used as the input data matrix. The integrated thermal desorption signals from the background samples
140   were used to derive the input error matrix. The best solution in each season was chosen according to
141   Q/Q_{exp}, the similarities between m/z profiles, time series, and diurnal variations of the factors. The
142   correlations between each factor and the measured key species, trace gas, and PM$_{2.5}$ were calculated
143   for better identification of the factors. It should be noted that there were also many peaks with m/z

144 below 100, but a large fraction of them was from thermal decomposition, and their inclusion would
145 add great complexity to the factor assignments. The signal intensity instead of the mass concentration
146 was used because sensitivity quantification of the TDCIMS was based on the calibration of limited
147 numbers of compounds which may induce unknown uncertainties when quantifying the sources. As a
148 result, the signal intensity measured by the TDCIMS is reported for reference and the relative
149 variations of detected species are studied rather than their estimated ambient concentrations.

2.3 Quantifying source and loss terms of UFP number concentrations.

151 In the measured size distribution plots, there are usually abrupt increases in UFP number concentration.
152 During new particle formation (NPF) periods, the abrupt increases of UFPs are usually accompanied
153 by a burst of sub-3 nm particles and usually start from noontime. During non-NPF periods, the abrupt
154 increases of UFPs are usually accompanied by an increase in primary emission tracers (as will be
155 shown in Section 3.2). We apply the GDE to quantify the new particle formation rates (J) and primary
156 particle number emission rates (E) at the observation site. The calculation of J follows those described
157 in previous studies (Cai and Jiang, 2017; Cai et al., 2017). The calculation of $E_{[i,j]}$ (m^{-3} s^{-1}), the particle
158 emission rates in the size range of [d_i, d_j], follows Eq. 1 (Cai et al., 2018; Kontkanen et al., 2020)
159 during non-NPF periods.

$$E_{[i,j]} = \frac{dN_{[i,j]}}{dt} + GR(n_j\text{-}n_i) + CoagSnk_{[i,j]} - CoagSrc_{[i,j]} - TR_{[i,j]} \qquad \text{(Eq. 1)}$$

161 Where $\dfrac{dN_{[i,j]}}{dt}$ (m^{-3} s^{-1}) is the variation of the particle number concentration in the size range of [d_i,

162 d_j] during the period of dt (s^{-1}); $GR(n_j\text{-}n_i)$ (m^{-3} s^{-1}) is the net condensation growth term, GR (m s^{-1}) is
163 the condensational growth rate of particle d_i, and n_i (m^{-4}) is the particle number size distribution
164 function for particle d_i; $CoagSrc_{[i,j]}$ and $CoagSnk_{[i,j]}$ (m^{-3} s^{-1}) are the coagulation source and sink terms;
165 $TR_{[i,j]}$ is the transport term. Overall, 33 size bins were included in the size range of 3-50 nm.

166 The term $\dfrac{dN_{[i,j]}}{dt}$ and $CoagSnk_{[i,j]}$ can be directly calculated from the size distribution data (Cai et al.,

167 2018). GR is calculated by the theoretical condensation of the condensable vapors, that is the sum of
168 H$_2$SO$_4$ and condensable organic vapor concentrations. Here, we regard condensable organic vapors as
169 oxygenated organic molecules (OOMs) with saturation vapor pressure lower than 0.3 μg m^{-3} as in our
170 previous studies (Li et al., 2022a; Qiao et al., 2021). Since not all the observation days were equipped
171 with the measurements of condensable vapors, we adopted seasonal-dependent GR derived from
172 seasonal average condensable vapor concentrations reported in our previous study, that is $1.2×10^7$,
173 $9.9×10^7$, $1.2×10^8$, and $5.0×10^7$ cm^{-3} for winter, spring, summer, and autumn (Qiao et al., 2021),
174 respectively. For particles smaller than 50 nm, $CoagSrc_{[i,j]}$ term can be neglected; for particles smaller
175 than 5 nm, the uncertainties will be very large for E. We only calculated E_{3-50} in this study and

176   *CoagSrc*$_{[i,j]}$ was thus neglected. Generally, *TR*$_{[i,j]}$ term cannot be quantified using the mathematic
177   method. As our previous study has indicated there was no significant transport term on a long-term
178   time scale (Kontkanen et al., 2020), we initially assumed that *TR*$_{[i,j]}$ equals 0. Another assumption is
179   that the influences from the variation in MLH are neglected. We briefly explore how the assumptions
180   of *TR*$_{[i,j]}$ and MLH influence the results in the next paragraph.

181   On the particle size distribution plots, we notice that the abrupt appearance of particles during non-
182   NPF days usually happens in the early morning (6:00-9:00) and late afternoon (17:00-20:00) (Figure
183   S1). The afternoon peak is accompanied by a decrease in MLH and an increase in particle numbers in
184   all sizes within the range of 3-50 nm, thus the abrupt increase in particle number concentration could
185   be due to the combined effects of MLH, transport, and emission. The morning peak is accompanied
186   by the increase in MLH, which should decrease particle number concentrations, and the increase in
187   particle number is only observed for 3-30 nm particles but not for 30-50 nm. Thus, the increasing
188   morning peak could only be caused by the primary emission of 3-30 nm particles. As a result, the 3-
189   30 nm particle emission rate during 6:00-9:00 is calculated to represent the average primary particle
190   emission rates for each day. It should be noted that the emission rates during 6:00-9:00 may be
191   underestimated due to the increase of MLH, and the emission rates only represent the increasing rates
192   of primary particles at the observational site, not the direct emission rates from the sources.

193   **3. Results and discussion**

194   **3.1 UFP concentration, composition, and seasonal variability**

195   The overall concentration of UFPs is the highest in winter and the lowest in summer. The UFP number
196   concentrations expressed in mean ± standard deviation are $(1.7\pm1.2)\times10^4$, $(1.5\pm1.1)\times10^4$,
197     $(1.1\pm0.7)\times10^4$, and $(1.5\pm0.9)\times10^4$ cm^{-3} (Figure 1a) and the UFP mass concentrations are 1.3±0.9,
198   1.2±0.9, 1.0±0.6, and 1.2±0.7 μg m^{-3} (Figure 1b) for winter, spring, summer, and autumn, respectively.
199   The seasonal variations are partly caused by the variation in MLH (Figure S2), while the other driving
200   factors are related to the source and loss terms of UFPs and will be further discussed in Section 3.3.
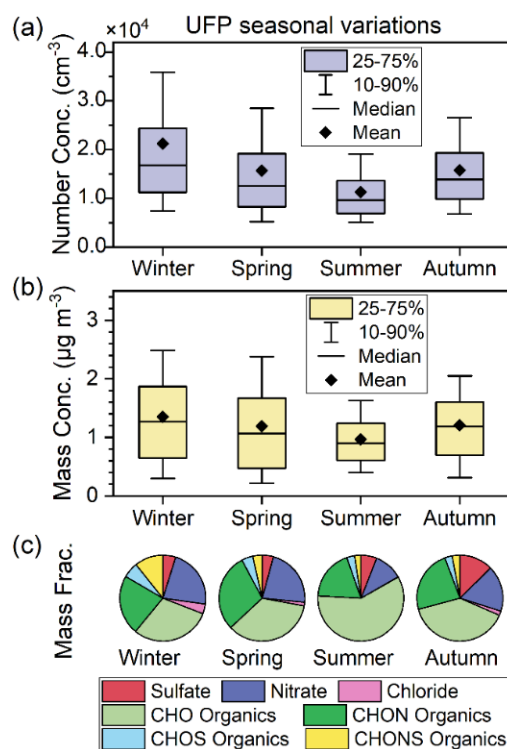
Figure 1. Seasonal variations of UFP concentrations and composition in urban Beijing. (a) UFP number concentrations in the size range of 3-100 nm. (b) UFP mass concentrations integrated from size distribution measurements, assuming spherical particles with a density of 1.4 g cm^{-3}. (c) Mass fractions of the components measured by the TDCIMS in negative ion mode.

The detected UFP composition is dominated by organics (68-81% for mass fraction), with minor contributions from nitrate (11-22%), sulfate (4-13%), and chloride (0.1-4%) over all four seasons (Figure 1c). The organic species include CHO, CHON, CHOS, and CHONS organics, contributing 30-59%, 19-29%, 3-6%, and 2-11% mass concentrations of the detected UFP compounds, respectively. The detected particulate species are similar for all four seasons as indicated by the similarities in the mass defect plots (Figure S3). The measured composition is consistent with the offline results from Beijing, which showed that organics were the most abundant in UFPs (Massling et al., 2009; Zhao et al., 2017). It should be noted that the collected mass integrated from the TDCIMS signals is ~50% of the total collected mass estimated from the size distributions (Figure S4). This is possibly due to the uncertainties in the quantification methods or because some UFP compounds (e.g., ammonia, amines, black carbon, and alkanes) cannot be ionized by O$_2^-$ in the TDCIMS. However, as the mass estimated from the two methods are in good correlation, we assume that the TDCIMS-measured composition is representative of UFP composition. As some of the particulate CHON, CHOS, and CHONS organics would decompose to CHO fragments in the TDCIMS during the thermal desorption process, there may be some underestimation of CHON and CHOS/CHONS organics and overestimation of CHO organics.

A major seasonal difference in UFP chemical composition is that the highest fractions of slow-

222   desorbed CHO organics are observed in summer (59%), which may be related to the strongest solar
223   radiation and lowest NO_x concentrations. On the one hand, the appearance of most CHO organic ions
224   during temperature ramping of the Pt wire occurs at higher temperatures compared to nitrate and
225   chloride, while at slightly lower temperatures compared to sulfate (Figure S5). The higher temperature
226   desorption, which we refer to as "slowly-desorbed," indicates that these species must be low-volatility
227   compounds or the corresponding thermal decomposition fragments. On the other hand, the overall
228   CHO organic mass has an afternoon peak at ~14:00, and its diurnal variation is consistent with that for
229   O_3 in summer (Figure S6), indicating they might be related to photooxidation chemistry. Based on
230   these, we hypothesize that CHO organics in the UFPs are mostly from the partitioning of low-volatility
231   compounds originating from the gas-phase oxidation. Thus, the higher CHO fractions in summer are
232   due to the strongest solar radiation, which benefits the gaseous photooxidation, and the lowest NO_x
233   (Figure S2), which contributes to the formation of CHO organics over CHON organics (Yan et al.,
234   2020; Ye et al., 2019).

235   Another seasonal difference is that higher fractions of fast-desorbed species are measured in winter,
236   including nitrate, chloride, and some CHON (e.g., $C_6H_4NO_3^-$, nitrophenols) organic compounds. These
237   species are all desorbed at lower temperatures (Figure S5) and their concentrations in UFPs are
238   negatively correlated to ambient temperature (Figure S7), indicating their relatively higher volatility.
239   Thus, the higher fractions in winter are mainly governed by the temperature-dependent partitioning of
240   these compounds. It should be noted that CHONS organic (e.g., deprotonated aminomethanesulfonic
241   acid $CH_4NSO_3^-$ and deprotonated taurine $C_2H_6NSO_3^-$) fractions also increase in winter. Previously,
242    $CH_4NSO_3^-$ and $C_2H_6NSO_3^-$ were reported to be formed in the gas phase through the reaction between
243   SO_3 and amines under dry conditions (Li et al., 2018; Sarkar et al., 2019). Their gaseous formation are
244   likely happen in winter Beijing due to the low ambient relative humidity. The seasonal variations of
245   these CHONS species are different from those in larger particles where S-containing organics are
246   mainly organosulfates from primary emissions or heterogeneous/aqueous reactions (Ma et al., 2022).

247   The composition of UFPs also varies greatly with particle size. As shown in Figure 2, the most
248   significant size-dependent variations were observed for nitrate and CHO organics. The nitrate fraction
249   increases significantly with increasing particle diameter, probably due to the Kelvin effects that prevent
250   it from partitioning to small particles, or due to an increase in aqueous/heterogeneous processes at
251   larger particle sizes. The CHO organic fraction decreases significantly with increased particle size,
252   possibly due to its low volatility that favors smaller particles compared to the high-volatility
253   compounds. Compared to CHO organics, the relative contributions of N- and S-containing organics
254   increase with particle size, possibly due to higher volatility or the aqueous/heterogeneous formation as
255   particles grow. The sulfate fraction does not change significantly with particle sizes, possibly due to
256   the opposite size-dependence of condensational growth of H_2SO_4 and the aqueous/heterogeneous
257   formation of sulfate.
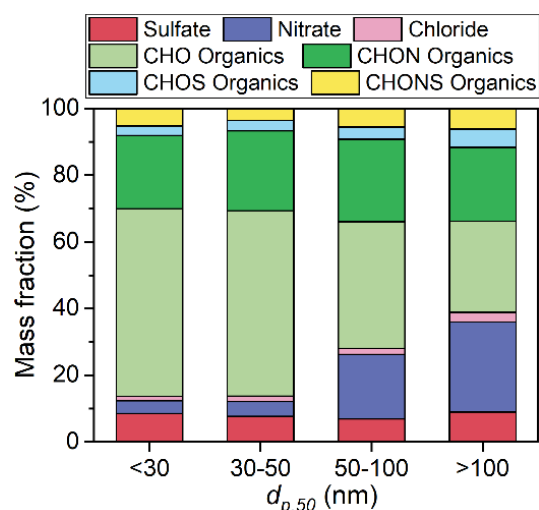
Figure 2. Size-dependent composition of UFPs. UFP composition mass fraction variation with the representing particle size $d_{p,50}$. $d_{p,50}$ corresponds to 50% volume mean diameter of particles collected on the TDCIMS filament.

3.2 Sources of UFP organics and their seasonal variabilities

As organics are the main components of UFPs, PMF source apportionments were performed for the organic compounds. Five factors were identified in each season. The factor profiles and their diurnal variations in winter are shown in Figure 3, and the results in other seasons are shown in Figure S8-10. The correlations between PMF factors and key UFP components, trace gases, meteorology parameters, and PM2.5 for the four seasons are shown in Figure S11.
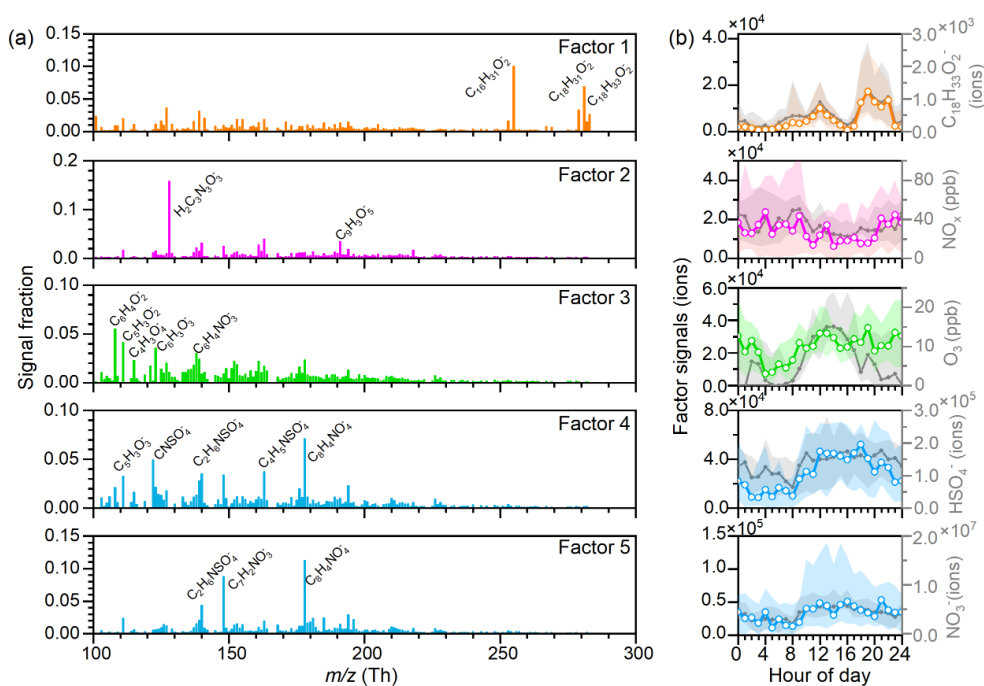
Figure 3. Source apportionment of the UFP organic composition (m/z 100-300) measured by the TDCIMS in winter. (a) m/z profiles of the five PMF factors; (b) diurnal variations of each factor and

271 their related terms.

272 Factor 1 and factor 2 are identified as cooking-related and vehicle-related sources, respectively. Factor
273 1 is enriched in $C_{16}H_{31}O_2^-$, $C_{18}H_{31}O_2^-$, and $C_{18}H_{33}O_2^-$ (assigned to deprotonated palmitic acid, linoleic
274 acid, and oleic acids, respectively). Previous studies have revealed that saturated and unsaturated fatty
275 acids are the major constituents in cooking emissions, accounting for 73-85% of the cooking organic
276 matter, among which palmitic acid and oleic acid can be treated as the unique fingerprints of
277 atmospheric cooking particles (Zhao et al., 2007b, a). Factor 1 and the tracers show clear morning,
278 noon, and evening peaks, corresponding to breakfast, lunch, and dinner times. Factor 2 is enriched in
279 $C_3N_3O_3H_2^-$ (assigned to deprotonated cyanuric acid). Cyanuric acid was previously found with the
280 biggest emission in the urea-based selective catalytic reduction (SCR) technology for the reduction of
281 NO_x from the exhaust of diesel-powered vehicles (Yassine et al., 2012). Factor 2 and the tracer show
282 clear morning peaks corresponding to the morning rush hours, consistent with the diurnal variation of
283 NO_x. These two factors are also identified in the other three seasons (Figure S8-10).

284 Besides these two primary sources, trace amounts of a biomass-burning tracer $C_6H_9O_5^-$ (assigned to
285 deprotonated levoglucosan) were also observed. However, its contribution to the total signal is small
286 and could not be separated into individual factors in the PMF analysis. We thus conclude that the
287 contribution of biomass burning to UFPs might be small in urban Beijing. This is understandable since
288 the burning of high-polluting fuels has been phased out in urban Beijing by the People's Government
289 of Beijing Municipality since 2014 (Municipality, 2014). Although large particles in urban Beijing
290 could be influenced by biomass burning and coal combustion through transport from surrounding
291 regions (Li et al., 2022b; Sun et al., 2015; Zhang et al., 2013; Zhang et al., 2008), UFPs could hardly
292 survive after long-distance transport due to their short lifetime.

293 Factors 3-5 are identified as secondary sources related to photooxidation formation or
294 aqueous/heterogeneous formation. In winter (Figure 3), factor 3 is enriched in slowly-desorbed, low-
295 volatility CHO organics and has daytime peaks at ~12:00-18:00, which is consistent with the diurnal
296 variation of O_3. They should come from gas-phase photooxidation followed by gas-particle
297 partitioning. Factor 4 and factor 5 are enriched in N- or S-containing organics. Their time series and
298 diurnal variability are highly correlated with sulfate, nitrate, $PM_{2.5}$, and relative humidity, indicating
299 the aqueous/heterogeneous formation pathway. Similarly, in spring and autumn, factor 3 is identified
300 as a photooxidation factor that is enriched in CHO organics, and factors 4-5 are identified as
301 aqueous/heterogeneous factors that are enriched in N- or S-containing organics (Figure S8-10).
302 Differently, in summer, factor 4 is identified as a photooxidation factor.

303 Clear seasonal variability of the sources was observed, with the contribution of primary emission
304 factors and aqueous/heterogeneous factors higher in winter and autumn, and the contribution of
305 photooxidation factors higher in summer (Figure S11). The sum of cooking and vehicle sources
306 contributed to 10-35% of the total organic signals in the m/z range of 100-300. The fractions of these

307 primary emissions are higher in winter and autumn, possibly indicating higher emissions. Another
308 possibility is that the oxidation degradation of these primary emissions is faster in summer and spring
309 due to higher oxidants and ambient temperature. The contributions of photooxidation factors are 20-
310 70% to the total organic signals in the m/z range of 100-300, with the highest in summer, and lowest
311 in winter. This is consistent with the highest CHO organic fractions in UFPs in summer in Figure 1
312 and is attributed to the strongest solar radiation. The contributions of aqueous/heterogeneous sources
313 are 15-60% to the total organic signals in the m/z range of 100-300, with the highest in winter and
314 lowest in summer.

315 To identify the sources for UFP numbers, we further combined the source analysis with variation in
316 particle size distributions. Among the identified four classes of composition sources, some are related
317 to the increase of UFP number concentrations, while others are related to the increase of UFP diameters.

318 The increase in UFP numbers is usually accompanied by the enhanced contribution of cooking- or
319 vehicle-related components or new particle formation events. An example is shown in Figure 4, a
320 relatively clean day with little interference from background aerosols. There are three periods where
321 UFP bursts were observed. During period 1, i.e., 6:00-9:00, a mode with a peak diameter at ~20 nm
322 appeared with a rapid increase in the vehicle tracer, $C_3N_3O_3H_2^-$. Compared to that before period 1, the
323 contribution of the vehicle-related factor increased from 7% to 25%. During period 2, i.e., 12:00-15:00,
324 new particle formation happens with a burst of particles at a peak diameter of 5-10 nm. Compared to
325 that before period 2, the contribution of the photooxidation-related factor increased from 64% to 92%.
326 This is consistent with our previous studies that slowly-desorbed CHO organics were the most
327 abundant compounds during NPF periods (Li et al., 2022a). During period 3, i.e., 18:00-22:00, a mode
328 with peak diameter at ~30 nm bursts, with a rapid increase in the cooking tracer, $C_{18}H_{31}O_2^-$. $C_{18}H_{31}O_2^-$
329 also has two minor peaks in the morning and noon time, consistent with the cooking activities.
330 Compared to that before period 3, the contribution of the cooking-related factor increased from 18%
331 to 67%. Thus, we conclude that the increase in UFP numbers in the three periods is mainly attributed
332 to the increase in vehicle emissions, new particle formations, and cooking emissions, respectively.
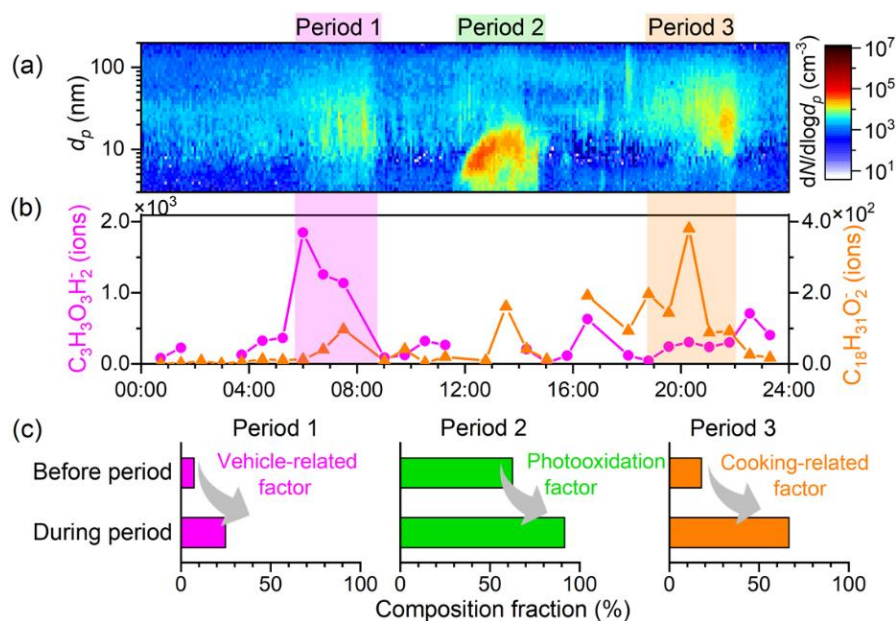
Figure 4. The particle number size distributions (a) and UFP composition variability (b-c) on April 16th, 2020. The three periods with the abrupt appearance of UFP particles on this day are identified as vehicle-related (period 1), NPF-related (period 2), and cooking-related (period 3) according to TDCIMS composition measurements.

The morning, noon, and evening peaks in UFP numbers were widely observed during the observation days in all four seasons. During non-NPF days, the UFP number concentration peak mainly appears in the morning and evening time, corresponding to the primary emissions, and we choose the morning periods to calculate the daily-averaged E. During NPF days, the UFP number peak mainly appears in the noon time, and the daily-averaged J was calculated during these periods. These further indicate that cooking emissions, vehicle emissions, and new particle formation are the main sources of UFP number concentrations.

Different from these three factors, the increased contribution of the aqueous/heterogeneous factor is not accompanied by the increase of UFP number concentrations but by the increase of UFP mode diameters. The contribution of aqueous/heterogeneous factor to sub-50 nm particles is only ~20%. For example, in the day presented in Figure 4, aqueous/heterogeneous factor accounted less than ~10% for the three bursts of UFP number concentration. However, it starts to dominate the organic composition when UFP particles grow above 50 nm (Figure S12), indicating an important role of aqueous/heterogeneous processes in the growth of particles larger than 50 nm in diameter.

3.3 Driving factors for the seasonal variability of UFPs.

As we have identified the main sources for UFP number concentrations in Section 3.2, we can further address the reasons for the significant seasonal differences in UFP number concentrations as has been shown in Figure 1, according to the variations in their sources and losses. The source terms mainly

include new particle formation rates (here represented by J_3) and primary emission rates (here represented by E_{3-50}); the loss terms are presented by condensational growth rates (GR_{3-50}) and coagulation sinks. Here, we apply the condensation sink (CS) to evaluate the strength of coagulation loss.

The main sources of the UFP number concentration, J_3, and E_{3-50}, are both higher in winter and lower in summer (Figure 5a-b), which are presumably caused by temperature effects. The temperature effect on J_3 is mainly due to the temperature-dependent cluster evaporation rates as reported in our previous study (Deng et al., 2020). This seasonal dependence of atmospheric UFPs attributed to vehicle emissions and its underlining reasons have not been revealed before. On the one hand, the low ambient temperature will largely increase the vehicle emission factors for particle numbers and gaseous hydrocarbons (Suarez-Bertoa and Astorga, 2018; Wen et al., 2021). On the other hand, a large fraction of the nanoparticles from vehicle emissions has been proposed to be formed by nucleation of the emitted hydrocarbon vapors or their oxidation products (Rönkkö and Timonen, 2019). The high ambient temperatures in summer may suppress the formation of these vehicle-related particles, just like it suppresses J_3 during ambient NPF.
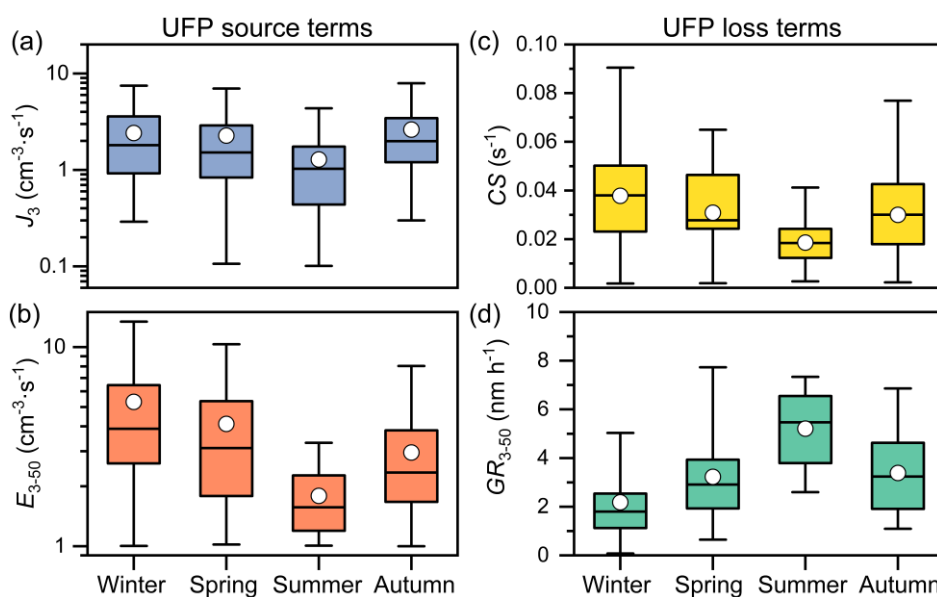
Figure 5. Seasonal variations of the main source and loss terms of UFP number concentration. (a) New particle formation rates for 3 nm particles (J_3); (b) daily average primary particle emission rates for 3-50 nm particles (E_{3-50}) during 6:00-9:00; (c) condensation sink (CS); (d) growth rates for 3-50 nm particles (GR_{3-50}) during new particle formation events using the mode fitting method.

The lowest GR of UFP occurs in winter (Figure 5d), which further contributes to high wintertime UFP number concentrations. CS and GR_{3-50} have opposite trends, with CS being the highest in winter while GR_{3-50} being the highest in summer (Figure 5c-d). The highest GR_{3-50} in summer is due to the highest condensable vapor concentrations in summer caused by strong solar radiation and high temperature

favoring the formation of condensable OOMs (Li et al., 2022a; Qiao et al., 2021). The theoretical condensational GR by OOMs and H_2SO_4 for 20 nm particles are 1.1, 3.0, 4.0, and 1.8 nm·h^{-1} in winter, spring, summer, and autumn, respectively, and they are close to GR_{3-50} derived during NPF events using the mode-fitting method as shown in Figure 5d. Under the observed average GR_{3-50}, the time needed for sub-3 nm to grow above 50 nm is the shortest in summer (~9 h) and the longest in winter (~24 h). Thus, the lower GR in winter also contributes to the highest UFP number concentrations in winter.

4. Conclusions

In this study, we explored the UFP composition and sources in typical polluted urban environments based on near-continuous measurements of UFP composition and size distributions in Beijing over four seasons. We observed that UFP composition varied with seasons and particle diameter, indicating their different sources. Specifically, photooxidation processes generate more CHO organics, leading to higher CHO fractions in summer. While aqueous/heterogeneous processes generate more N- and S-containing organics, leading to higher N- and S-containing organic fractions in above-50 nm particles than sub-50 nm particles. Combining the PMF analysis for UFP organics and the size distribution analysis, we found that vehicle and cooking emissions are two of the most important primary sources of UFP number concentrations in urban Beijing, while new particle formation is the most important secondary source of UFP number concentrations and would increase the contribution of CHO organics to UFP composition. The aqueous/heterogeneous sources would not increase UFP number concentration but would increase UFP mode diameters and mass concentrations. For the seasonal variations, we found that UFP number concentrations are the highest in winter. This is mainly due to the highest primary particle emissions, the highest new particle formation rates, and the lowest particle growth rates in winter. Further controlling of UFPs in urban Beijing needs to focus on vehicle emissions, and the gas precursors related to secondary sources of UFPs.

The observed distinct seasonal variabilities of UFP composition and their size dependence emphasize the importance of long-term and high-time-resolution measurements of both UFP composition and size distributions. This could provide valuable datasets for the evaluation of UFP's long-term exposure risks. The high time-resolution measurements combined with PMF analysis can also help identify the secondary UFP sources, which contribute the major fraction of organic signals but could not be identified from previous offline UFP measurements. Further addressing the UFP composition and sources on the regional scale still requires measurements at sites with different distances from the emission sources due to the short lifetime of UFPs.

Data availability.

Data are available upon request from the corresponding authors.

Supplement.

The contents of the supporting information include the diurnal variations of E_{3-50} during non-NPF days over four seasons (Figure S1); the diurnal variations of MLH, UVB, T, RH, O_3, NO_x, and $PM_{2.5}$ in the four seasons (Figure S2); details of the measured UFP composition during four seasons (Figure S3); seasonal variation of the UFP mass estimated from TDCIMS and PSD (Figure S4); the averaged thermal desorption profiles of different UFP composition (Figure S5); the diurnal variation of CHO organics in the four seasons (Figure S6); temperature dependence of some fast-desorbed UFP composition (Figure S7); the spectra of five PMF-factors during spring, summer, and autumn (Figure S8-10); summary of PMF factors during the four seasons (Figure S11); the contribution of different factors as a function of particle sizes (Figure S12); summary of sampling periods (Table S1).

Author contributions.

XL, JJ, and JS designed the study. XL, YC, YYL, RC, YRL, and CD participated in data collection and performed the data analysis. XL prepared the manuscript with contributions from all co-authors. All authors approved the final version of the manuscript.

Competing interests.

The authors declare that they have no conflict of interest.

References

Cabada, J. C., Rees, S., Takahama, S., Khlystov, A., Pandis, S. N., Davidson, C. I., and Robinson, A. L.: Mass size distributions and size resolved chemical composition of fine particulate matter at the Pittsburgh supersite, Atmos. Environ., 38, 3127-3141, 10.1016/j.atmosenv.2004.03.004, 2004.

Cai, R., and Jiang, J.: A new balance formula to estimate new particle formation rate: reevaluating the effect of coagulation scavenging, Atmos. Chem. Phys., 17, 12659-12675, 2017.

Cai, R., Yang, D., Fu, Y., Wang, X., Li, X., Ma, Y., Hao, J., Zheng, J., and Jiang, J.: Aerosol surface area concentration: a governing factor in new particle formation in Beijing, Atmos. Chem. Phys., 17,

444 12327, 2017.

445 Cai, R., Chandra, I., Yang, D., Yao, L., Fu, Y., Li, X., Lu, Y., Luo, L., Hao, J., Ma, Y., Wang, L., Zheng,
446 J., Seto, T., and Jiang, J.: Estimating the influence of transport on aerosol size distributions during new
447 particle formation events, Atmos. Chem. Phys., 18, 16587-16599, 10.5194/acp-18-16587-2018, 2018.

448 Canonaco, F., Crippa, M., Slowik, J., Baltensperger, U., and Prévôt, A.: SoFi, an IGOR-based interface
449 for the efficient use of the generalized multilinear engine (ME-2) for the source apportionment: ME-2
450 application to aerosol mass spectrometer data, Atmos. Meas. Tech., 6, 3649, 2013.

451 Cass, G. R., Hughes, L. A., Bhave, P., Kleeman, M. J., Allen, J. O., and Salmon, L. G.: The chemical
452 composition of atmospheric ultrafine particles, Philosophical Transactions of the Royal Society of
453 London Series a-Mathematical Physical and Engineering Sciences, 358, 2581-2592,
454 10.1098/rsta.2000.0670, 2000.

455 Deng, C., Fu, Y., Dada, L., Yan, C., Cai, R., Yang, D., Zhou, Y., Yin, R., Lu, Y., Li, X., Qiao, X., Fan,
456 X., Nie, W., Kontkanen, J., Kangasluoma, J., Chu, B., Ding, A., Kerminen, V.-M., Paasonen, P.,
457 Worsnop, D. R., Bianchi, F., Liu, Y., Zheng, J., Wang, L., Kulmala, M., and Jiang, J.: Seasonal
458 Characteristics of New Particle Formation and Growth in Urban Beijing, Environ. Sci. Technol., 54,
459 8547–8557, 10.1021/acs.est.0c00808, 2020.

460 Eresmaa, N., Harkonen, J., Joffre, S. M., Schultz, D. M., Karppinen, A., and Kukkonen, J.: A Three-
461 Step Method for Estimating the Mixing Height Using Ceilometer Data from the Helsinki Testbed,
462 Journal of Applied Meteorology and Climatology, 51, 2172-2187, 10.1175/jamc-d-12-058.1, 2012.

463 Glicker, H. S., Lawler, M. J., Ortega, J., de Sá, S. S., Martin, S. T., Artaxo, P., Vega Bustillos, O., de
464 Souza, R., Tota, J., Carlton, A., and Smith, J. N.: Chemical composition of ultrafine aerosol particles
465 in central Amazonia during the wet season, Atmos. Chem. Phys., 19, 13053-13066, 10.5194/acp-19-
466 13053-2019, 2019.

467 Ham, W. A., and Kleeman, M. J.: Size-resolved source apportionment of carbonaceous particulate
468 matter in urban and rural sites in central California, Atmos. Environ., 45, 3988-3995,
469 10.1016/j.atmosenv.2011.04.063, 2011.

470 Understanding the Health Effects of Ambient Ultrafine Particles:
471 https://www.healtheffects.org/publication/understanding-health-effects-ambient-ultrafine-particles,
472 access: Jan 26th, 2019, 2013.

473 Herner, J. D., Aw, J., Gao, O., Chang, D. P., and Kleeman, M. J.: Size and composition distribution of
474 airborne particulate matter in northern California: I-particulate mass, carbon, and water-soluble ions,
475 J. Air Waste Manage., 55, 30-51, 10.1080/10473289.2005.10464600, 2005.

476 Hu, W., Hu, M., Hu, W.-W., Zheng, J., Chen, C., Wu, Y., and Guo, S.: Seasonal variations in high time-
477 resolved chemical compositions, sources, and evolution of atmospheric submicron aerosols in the
478 megacity Beijing, Atmos. Chem. Phys., 17, 9979-10000, 10.5194/acp-17-9979-2017, 2017.

479 Kleeman, M. J., Riddle, S. G., Robert, M. A., Jakober, C. A., Fine, P. M., Hays, M. D., Schauer, J. J.,
480 and Hannigan, M. P.: Source Apportionment of Fine (PM1.8) and Ultrafine (PM0.1) Airborne
481 Particulate Matter during a Severe Winter Pollution Episode, Environ. Sci. Technol., 43, 272-279,
482 10.1021/es800400m, 2009.

483 Kontkanen, J., Deng, C., Fu, Y., Dada, L., Zhou, Y., Cai, J., Daellenbach, K. R., Hakala, S., Kokkonen,
484 T. V., Lin, Z., Liu, Y., Wang, Y., Yan, C., Petäjä, T., Jiang, J., Kulmala, M., and Paasonen, P.: Size-

485 resolved particle number emissions in Beijing determined from measured particle size distributions,
486 Atmos. Chem. Phys., 20, 11329-11348, 10.5194/acp-20-11329-2020, 2020.

487 Kulmala, M., Vehkamäki, H., Petäjä, T., Dal Maso, M., Lauri, A., Kerminen, V. M., Birmili, W., and
488 McMurry, P. H.: Formation and growth rates of ultrafine atmospheric particles: a review of
489 observations, J. Aerosol. Sci., 35, 143–176, 10.1016/j.jaerosci.2003.10.003, 2004.

490 Lawler, M. J., Whitehead, J., O'Dowd, C., Monahan, C., McFiggans, G., and Smith, J. N.: Composition
491 of 15-85 nm particles in marine air, Atmos. Chem. Phys., 14, 11557–11569, 10.5194/acp-14-11557-
492 2014, 2014.

493 Lawler, M. J., Rissanen, M. P., Ehn, M., Mauldin, R. L., Sarnela, N., Sipilä, M., and Smith, J. N.:
494 Evidence for Diverse Biogeochemical Drivers of Boreal Forest New Particle Formation, Geophys. Res.
495 Lett., 45, 2038–2046, doi:10.1002/2017GL076394, 2018.

496 Lawler, M. J., Draper, D. C., and Smith, J. N.: Atmospheric fungal nanoparticle bursts, Sci. Adv., 6,
497 No. eaax9051, 10.1126/sciadv.aax9051, 2020.

498 Lawler, M. J., Saltzman, E. S., Karlsson, L., Zieger, P., Salter, M., Baccarini, A., Schmale, J., and Leck,
499 C.: New Insights Into the Composition and Origins of Ultrafine Aerosol in the Summertime High
500 Arctic, Geophys. Res. Lett., 48, 10.1029/2021gl094395, 2021.

501 Li, H., Zhong, J., Vehkamaki, H., Kurten, T., Wang, W., Ge, M., Zhang, S., Li, Z., Zhang, X., Francisco,
502 J. S., and Zeng, X. C.: Self-Catalytic Reaction of SO3 and NH3 To Produce Sulfamic Acid and Its
503 Implication to Atmospheric Particle Formation, J. Am. Chem. Soc., 140, 11020-11028,
504 10.1021/jacs.8b04928, 2018.

505 Li, X., Zhao, B., Zhou, W., Shi, H., Yin, R., Cai, R., Yang, D., Dallenbach, K., Deng, C., Fu, Y., Qiao,
506 X., Wang, L., Liu, Y., Yan, C., Kulmala, M., Zheng, J., Hao, J., Wang, S., and Jiang, J.: Responses of
507 gaseous sulfuric acid and particulate sulfate to reduced SO2 concentration: A perspective from long-
508 term measurements in Beijing, Sci. Total Environ., 721, No. 137700, 10.1016/j.scitotenv.2020.137700,
509 2020.

510 Li, X., Li, Y., Lawler, M. J., Hao, J., Smith, J. N., and Jiang, J.: Composition of Ultrafine Particles in
511 Urban Beijing: Measurement Using a Thermal Desorption Chemical Ionization Mass Spectrometer,
512 Environ. Sci. Technol., 55, 2859–2868, 10.1021/acs.est.0c06053, 2021.

513 Li, X., Li, Y., Cai, R., Yan, C., Qiao, X., Guo, Y., Deng, C., Yin, R., Chen, Y., Li, Y., Yao, L., Sarnela,
514 N., Zhang, Y., Petäjä, T., Bianchi, F., Liu, Y., Kulmala, M., Hao, J., Smith, J. N., and Jiang, J.:
515 Insufficient Condensable Organic Vapors Lead to Slow Growth of New Particles in an Urban
516 Environment, Environ. Sci. Technol., 55, 9936-9946, 10.1021/acs.est.2c01566, 2022a.

517 Li, X., Sun, N., Jin, Q., Zhao, Z., Wang, L., Wang, Q., Gu, X., Li, Y., and Liu, X.: Light absorption
518 properties of black and brown carbon in winter over the North China Plain: Impacts of regional
519 biomass burning, Atmos. Environ., 278, 10.1016/j.atmosenv.2022.119100, 2022b.

520 Liu, Y., Yan, C., Feng, Z., Zheng, F., Fan, X., Zhang, Y., Li, C., Zhou, Y., Lin, Z., Guo, Y., Zhang, Y.,
521 Ma, L., Zhou, W., Liu, Z., Dada, L., Daellenbach, K., Kontkanen, J., Cai, R., Chan, T., and Kulmala,
522 M.: Continuous and comprehensive atmospheric observations in Beijing: a station to understand the
523 complex urban atmospheric environment, Big Earth Data, 4, 295-321,
524 10.1080/20964471.2020.1798707, 2020.

525 Ma, J., Ungeheuer, F., Zheng, F., Du, W., Wang, Y., Cai, J., Zhou, Y., Yan, C., Liu, Y., Kulmala, M.,

Daellenbach, K. R., and Vogel, A. L.: Nontarget Screening Exhibits a Seasonal Cycle of PM2.5 Organic Aerosol Composition in Beijing, Environ. Sci. Technol., 10.1021/acs.est.1c06905, 2022.

Massling, A., Stock, M., Wehner, B., Wu, Z. J., Hu, M., Brueggemann, E., Gnauk, T., Herrmann, H., and Wiedensohler, A.: Size segregated water uptake of the urban submicrometer aerosol in Beijing, Atmos. Environ., 43, 1578-1589, 10.1016/j.atmosenv.2008.06.003, 2009.

Municipality, t. P. s. G. o. B.: The implementation of forbidden area for high-polluting fuels in Beijing, http://www.beijing.gov.cn/zhengce/zfwj/zfwj/szfwj/201905/t20190523_72669.html, 2014.

Oberdorster, G., Oberdorster, E., and Oberdorster, J.: Nanotoxicology: an emerging discipline evolving from studies of ultrafine particles, Environ Health Perspect, 113, 823-839, 10.1289/ehp.7339, 2005.

Ohlwein, S., Kappeler, R., Kutlar Joss, M., Kunzli, N., and Hoffmann, B.: Health effects of ultrafine particles: a systematic literature review update of epidemiological evidence, Int J Public Health, 64, 547-559, 10.1007/s00038-019-01202-7, 2019.

Organization, W. H.: WHO global air quality guidelines: particulate matter (PM2.5 and PM10), ozone, nitrogen dioxide, sulfur dioxide and carbon monoxide, https://apps.who.int/iris/bitstream/handle/10665/345329/9789240034228-eng.pdf, 2021.

Pierce, J. R., and Adams, P. J.: Efficiency of cloud condensation nuclei formation from ultrafine particles, Atmos. Chem. Phys., 7, 1367-1379, 2007.

Qiao, X., Yan, C., Li, X., Guo, Y., Yin, R., Deng, C., Li, C., Nie, W., Wang, M., Cai, R., Huang, D., Wang, Z., Yao, L., Worsnop, D. R., Bianchi, F., Liu, Y., Donahue, N. M., Kulmala, M., and Jiang, J.: Contribution of Atmospheric Oxygenated Organic Compounds to Particle Growth in an Urban Environment, Environ. Sci. Technol., 55, 13646–13656, 10.1021/acs.est.1c02095, 2021.

Rönkkö, T., and Timonen, H.: Overview of Sources and Characteristics of Nanoparticles in Urban Traffic-Influenced Areas, Journal of Alzheimer's Disease, 72, 1-14, 10.3233/JAD-190170, 2019.

Sarkar, S., Oram, B. K., and Bandyopadhyay, B.: Influence of Ammonia and Water on the Fate of Sulfur Trioxide in the Troposphere: Theoretical Investigation of Sulfamic Acid and Sulfuric Acid Formation Pathways, J. Phys. Chem. A., 123, 3131-3141, 10.1021/acs.jpca.8b09306, 2019.

Smith, J. N., Moore, K. F., McMurry, P. H., and Eisele, F. L.: Atmospheric measurements of sub-20 nm diameter particle chemical composition by thermal desorption chemical ionization mass spectrometry, Aerosol Sci. Tech., 38, 100–110, 10.1080/02786820490249036, 2004.

Smith, J. N., Moore, K. F., Eisele, F. L., Voisin, D., Ghimire, A. K., Sakurai, H., and McMurry, P. H.: Chemical composition of atmospheric nanoparticles during nucleation events in Atlanta, J. Geophys. Res-Atmos., 110, No. D22S03, 10.1029/2005jd005912, 2005.

Smith, J. N., Dunn, M. J., VanReken, T. M., Iida, K., Stolzenburg, M. R., McMurry, P. H., and Huey, L. G.: Chemical composition of atmospheric nanoparticles formed from nucleation in Tecamac, Mexico: Evidence for an important role for organic species in nanoparticle growth, Geophys. Res. Lett., 35, No. L4808, 10.1029/2007gl032523, 2008.

Smith, J. N., Barsanti, K. C., Friedli, H. R., Ehn, M., Kulmala, M., Collins, D. R., Scheckman, J. H., Williams, B. J., and McMurry, P. H.: Observations of aminium salts in atmospheric nanoparticles and possible climatic implications, Proc. Natl. Acad. Sci. U.S.A., 107, 6634–6639, 10.1073/pnas.0912127107, 2010.

Suarez-Bertoa, R., and Astorga, C.: Impact of cold temperature on Euro 6 passenger car emissions,

Environ. Pollut., 234, 318-329, 10.1016/j.envpol.2017.10.096, 2018.

Sun, Y., Xu, W., Zhang, Q., Jiang, Q., Canonaco, F., Prévôt, A. S. H., Fu, P., Li, J., Jayne, J., Worsnop, D. R., and Wang, Z.: Source apportionment of organic aerosol from 2-year highly time-resolved measurements by an aerosol chemical speciation monitor in Beijing, China, Atmos. Chem. Phys., 18, 8469-8489, 10.5194/acp-18-8469-2018, 2018.

Sun, Y. L., Wang, Z. F., Du, W., Zhang, Q., Wang, Q. Q., Fu, P. Q., Pan, X. L., Li, J., Jayne, J., and Worsnop, D. R.: Long-term real-time measurements of aerosol particle composition in Beijing, China: seasonal variations, meteorological effects, and source analysis, Atmos. Chem. Phys., 15, 10149-10165, 10.5194/acp-15-10149-2015, 2015.

Wen, Y., Zhang, S., He, L., Yang, S., Wu, X., and Wu, Y.: Characterizing start emissions of gasoline vehicles and the seasonal, diurnal and spatial variabilities in China, Atmos. Environ., 245, 10.1016/j.atmosenv.2020.118040, 2021.

WHO: Review of evidence on health aspects of air pollution — REVIHAAP. World Health Organisation, World Health Organisation, Regional Office for Europe, https://www.euro.who.int/__data/assets/pdf_file/0020/182432/e96762-final.pdf, 2013.

Winkler, P. M., Ortega, J., Karl, T., Cappellin, L., Friedli, H. R., Barsanti, K., McMurry, P. H., and Smith, J. N.: Identification of the biogenic compounds responsible for size-dependent nanoparticle growth, Geophys. Res. Lett., 39, No. L20815, 10.1029/2012gl053253, 2012.

Wu, Z., Hu, M., Liu, S., Wehner, B., Bauer, S., Ma ßling, A., Wiedensohler, A., Petäjä, T., Dal Maso, M., and Kulmala, M.: New particle formation in Beijing, China: Statistical analysis of a 1-year data set, J. Geophys. Res., 112, 10.1029/2006jd007406, 2007.

Xu, S., Ren, L., Lang, Y., Hou, S., Ren, H., Wei, L., Wu, L., Deng, J., Hu, W., Pan, X., Sun, Y., Wang, Z., Su, H., Cheng, Y., and Fu, P.: Molecular markers of biomass burning and primary biological aerosols in urban Beijing: size distribution and seasonal variation, Atmos. Chem. Phys., 20, 3623-3644, 10.5194/acp-20-3623-2020, 2020.

Xue, J., Xue, W., Sowlat, M. H., Sioutas, C., Lolinco, A., Hasson, A., and Kleeman, M. J.: Seasonal and Annual Source Appointment of Carbonaceous Ultrafine Particulate Matter (PM0.1) in Polluted California Cities, Environ. Sci. Technol., 53, 39-49, 10.1021/acs.est.8b04404, 2019.

Xue, W., Xue, J., Mousavi, A., Sioutas, C., and Kleeman, M. J.: Positive matrix factorization of ultrafine particle mass (PM0.1) at three sites in California, Sci. Total Environ., 715, 10.1016/j.scitotenv.2020.136902, 2020a.

Xue, W., Xue, J., Shirmohammadi, F., Sioutas, C., Lolinco, A., Hasson, A., and Kleeman, M. J.: Day-of-week patterns for ultrafine particulate matter components at four sites in California, Atmos. Environ., 222, 10.1016/j.atmosenv.2019.117088, 2020b.

Yan, C., Nie, W., Vogel, A. L., Dada, L., Lehtipalo, K., Stolzenburg, D., Wagner, R., Rissanen, M. P., Xiao, M., Ahonen, L., Fischer, L., Rose, C., Bianchi, F., Gordon, H., Simon, M., Heinritzi, M., Garmash, O., Roldin, P., Dias, A., Ye, P., Hofbauer, V., Amorim, A., Bauer, P. S., Bergen, A., Bernhammer, A. K., Breitenlechner, M., Brilke, S., Buchholz, A., Mazon, S. B., Canagaratna, M. R., Chen, X., Ding, A., Dommen, J., Draper, D. C., Duplissy, J., Frege, C., Heyn, C., Guida, R., Hakala, J., Heikkinen, L., Hoyle, C. R., Jokinen, T., Kangasluoma, J., Kirkby, J., Kontkanen, J., Kuerten, A., Lawler, M. J., Mai, H., Mathot, S., Mauldin, R. L., III, Molteni, U., Nichman, L., Nieminen, T., Nowak,

608   J., Ojdanic, A., Onnela, A., Pajunoja, A., Petaja, T., Piel, F., Quelever, L. L. J., Sarnela, N., Schallhart,

609   S., Sengupta, K., Sipila, M., Tome, A., Troestl, J., Vaisanen, O., Wagner, A. C., Ylisirnio, A., Zha, Q.,

610   Baltensperger, U., Carslaw, K. S., Curtius, J., Flagan, R. C., Hansel, A., Riipinen, I., Smith, J. N.,

611   Virtanen, A., Winkler, P. M., Donahue, N. M., Kerminen, V. M., Kulmala, M., Ehn, M., and Worsnop,

612   D. R.: Size-dependent influence of NOx on the growth rates of organic aerosol particles, Sci. Adv., 6,

613   eaay4945, 10.1126/sciadv.aay4945, 2020.

614   Yassine, M. M., Dabek-Zlotorzynska, E., and Celo, V.: Development of a hydrophilic interaction liquid

615   chromatography-mass spectrometry method for detection and quantification of urea thermal

616   decomposition by-products in emission from diesel engine employing selective catalytic reduction

617   technology, Journal of Chromatography A, 1229, 208-215, 10.1016/j.chroma.2012.01.046, 2012.

618   Ye, Q., Wang, M., Hofbauer, V., Stolzenburg, D., Chen, D., Schervish, M., Vogel, A., Mauldin, R. L.,

619   Baalbaki, R., Brilke, S., Dada, L., Dias, A., Duplissy, J., El Haddad, I., Finkenzeller, H., Fischer, L.,

620   He, X., Kim, C., Kuerten, A., Lamkaddam, H., Lee, C. P., Lehtipalo, K., Leiminger, M., Manninen, H.

621   E., Marten, R., Mentler, B., Partoll, E., Petaja, T., Rissanen, M., Schobesberger, S., Schuchmann, S.,

622   Simon, M., Tham, Y. J., Vazquez-Pufleau, M., Wagner, A. C., Wang, Y., Wu, Y., Xiao, M.,

623   Baltensperger, U., Curtius, J., Flagan, R., Kirkby, J., Kulmala, M., Volkamer, R., Winkler, P. M.,

624   Worsnop, D., and Donahue, N. M.: Molecular Composition and Volatility of Nucleated Particles from

625   alpha-Pinene Oxidation between-50 degrees C and+25 degrees C, Environ. Sci. Technol., 53, 12357–

626   12365, 10.1021/acs.est.9b03265, 2019.

627   Zhang, R., Jing, J., Tao, J., Hsu, S. C., Wang, G., Cao, J., Lee, C. S. L., Zhu, L., Chen, Z., Zhao, Y.,

628   and Shen, Z.: Chemical characterization and source apportionment of PM2.5 in Beijing: seasonal

629   perspective, Atmos. Chem. Phys., 13, 7053-7074, 10.5194/acp-13-7053-2013, 2013.

630   Zhang, T., Claeys, M., Cachier, H., Dong, S., Wang, W., Maenhaut, W., and Liu, X.: Identification and

631   estimation of the biomass burning contribution to Beijing aerosol using levoglucosan as a molecular

632   marker, Atmos. Environ., 42, 7013-7021, 10.1016/j.atmosenv.2008.04.050, 2008.

633   Zhao, P., Chen, Y., and Su, J.: Size-resolved carbonaceous components and water-soluble ions

634   measurements of ambient aerosol in Beijing, J. Environ. Sci., 54, 298-313, 10.1016/j.jes.2016.08.027,

635   2017.

636   Zhao, Y., Hu, M., Slanina, S., and Zhang, Y.: The molecular distribution of fine particulate organic

637   matter emitted from Western-style fast food cooking, Atmos Environ, 41, 8163-8171,

638   10.1016/j.atmosenv.2007.06.029, 2007a.

639   Zhao, Y., Hu, M., Slanina, S., and Zhang, Y.: Chemical compositions of fine particulate organic matter

640   emitted from Chinese cooking, Environ Sci Technol, 41, 99-105, 10.1021/es0614518, 2007b.

641